Laser-induced magnetization dynamics in a van der Waals ferromagnetic $Cr_2Ge_2Te_6$ nanoflake Ⓕ

Tongyao Zhang �id, Yuansen Chen, Yanxu Li, Zhichao Guo, Zhi Wang, Zheng Han, Wei He �id, and Jing Zhang

COLLECTIONS

Ⓕ   This paper was selected as Featured

View Online   Export Citation   CrossMark

Laser-induced magnetization dynamics in a van der Waals ferromagnetic Cr₂Ge₂Te₆ nanoflake

Tongyao Zhang,[1,2] Yuansen Chen,[1,2,a),b)] Yanxu Li,[1,2] Zhichao Guo,[1,2] Zhi Wang,[3,4] Zheng Han,[1,2] Wei He,[5,a)] and Jing Zhang[1,2]

AFFILIATIONS

[1]State Key Laboratory of Quantum Optics and Quantum Optics Devices, Institute of Opto-Electronics, Shanxi University, Taiyuan, Shanxi 030006, People's Republic of China

[2]Collaborative Innovation Center of Extreme Optics, Shanxi University, Taiyuan, Shanxi 030006, People's Republic of China

[3]Shenyang National Laboratory for Materials Science, Institute of Metal Research, Chinese Academy of Sciences, Shenyang 110016, People's Republic of China

[4]School of Material Science and Engineering, University of Science and Technology of China, Anhui 230026, China

[5]State Key Laboratory of Magnetism, Institute of Physics, Chinese Academy of Science, Beijing 100190, People's Republic of China

[a)]Authors to whom correspondence should be addressed: hewei@iphy.ac.cn and yuansen.chen@attocube.com
[b)]Present address: Attocube Systems AG, Eglfinger Weg 2, D-85540 Haar bei München, Germany.

ABSTRACT

Laser-induced magnetization dynamics is quantitatively investigated in a van der Waals ferromagnetic Cr₂Ge₂Te₆ nanoflake by means of time-resolved Faraday rotation. Under ferromagnetic resonance conditions, the angular dependence of spin precession dynamics gives rise to a perpendicular magnetic anisotropy with an effective field of 125 ± 8 mT. We further determine the field dependence of the effective damping coefficient, which is dominated by the inhomogeneous broadening of magnetic anisotropy in the regime of a small magnetic field while it diminishes to an intrinsic value of 0.006 ± 0.002 at high fields.

Published under license by AIP Publishing. https://doi.org/10.1063/5.0006080

Semiconductor spintronics promises applications in information processing of the next generation.[1] Semiconductor spin-based quantum systems have led to numerous discoveries, such as the spin Hall effect,[2,3] spin-helix states,[4,5] the quantum spin Hall effect,[6] the quantum anomalous Hall effect,[7] and Majorana particles.[8] Moreover, scalability and electrical tunability make these solid systems particularly interesting for quantum computing. Two-dimensional (2D) van der Waals (vdW) semiconductors represent a promising alternative in semiconductor spintronics.[9] Compared with epitaxially grown semiconductor quantum systems, 2D vdW semiconductors are easier to fabricate by mechanical exfoliation and offer strong intrinsic quantum confinement. In addition, the thickness of 2D materials can be precisely controlled with monolayer accuracy. In such vdW structures, atomic layers can be artificially stacked with controllable orientation, thereby allowing the crystal symmetry to be tuned as desired. This unique property allows flexible engineering of the electronic band structure, either by controlling the number of layers or by stacking heterostructures of different 2D materials. The number of layers determines the symmetry along the confinement direction, which

drastically affects the energy levels of spin subbands and valley subbands.[10] As a result, numerous spin-related phenomena have been observed in 2D atomic crystals, such as giant magnetoresistance,[11] the spin or valley Hall effect,[12,13] and spin–orbit torque.[14,15] Of more interest is the recent discovery of a 2D ferromagnet in which the ferromagnetism depends strongly on the number of layers,[16,17] which prompted measurements of the anomalous Hall effect.[18] Furthermore, the electrical control of ferromagnetism was experimentally demonstrated in different 2D systems,[19–21] an example of which is our recent work that demonstrates optically addressed electrical tunability of ferromagnetism in vdW semi-insulating Cr₂G₂Te₆.[21]

Here, we study magnetization dynamics in a nanoflake Cr₂Ge₂Te₆ by means of a two-color time-resolved Faraday rotation (TRFR) with a picosecond time resolution at cryogenic temperature. Below the Curie temperature, a pump beam of femtosecond pulses intensively heats the ferromagnet to produce instantaneous demagnetization and trigger the magnetization precession. By monitoring laser-induced magnetization dynamics in an external magnetic field H_{ext}, we determine the angular dependence of the precession

frequency and the transverse spin relaxation time. The precession frequency can be well fitted by the Kittel formula with an effective perpendicular anisotropic (PMA) magnetic field of $\mu_0 H_k = 125 \pm 8$ mT. By evaluating the field dependence of the spin relaxation rate, we propose that the effective damping coefficient α_{eff} in the regime of a small H_{ext} is dominated by inhomogeneous broadening due to PMA spatial fluctuations, and it diminishes to an intrinsic coefficient $\alpha_0 = 0.006 \pm 0.002$ at higher H_{ext}.

The sample investigated is a $Cr_2Ge_2Te_6$ flake exfoliated from a single crystal and encapsulated between two hexagonal boron nitride (h-BN) flakes on a fused silica substrate. To avoid degradation of the nanoflake, the whole sample fabrication is performed in a nitrogen-purged glovebox. Figure 1(a) shows a schematic description of the stacked structure, and Fig. 1(b) presents an optical micrograph showing the measurement area by the solid circle. Based on the scanning topography characterization presented in Fig. 1(c), the sample thickness is determined to be 10.5 nm. The inset of Fig. 1(c) shows the unit cell of $Cr_2Ge_2Te_6$, in which the ferromagnetism is due to the labeled Cr atoms.

The sample is mounted in a helium-free cryostat, and all measurements presented in this Letter are done at a sample temperature of 10 K, which is well below the Curie temperature of $Cr_2Ge_2Te_6$.[22] We first measure the magnetization hysteresis loops by using magneto-optic Kerr rotation in Faraday geometry. More technical details are described in our previous work.[21] We define θ_H as the angle between $\mathbf{H}_{ext}$ and the sample normal (i.e., $\theta_H = 0°$ in this configuration). As shown in Fig. 1(d), the out-of-plane coercivity of the $Cr_2Ge_2Te_6$ investigated is determined as $H_c(0°) = 8.0 \pm 0.1$ mT. This coercivity is similar to the values previously reported for similar samples from 3.5 to 20 nm thick.[21]

The sample normal is rotated through the angle θ_H with respect to $\mathbf{H}_{ext}$, which is always perpendicular to the optical axis. Hereinafter,
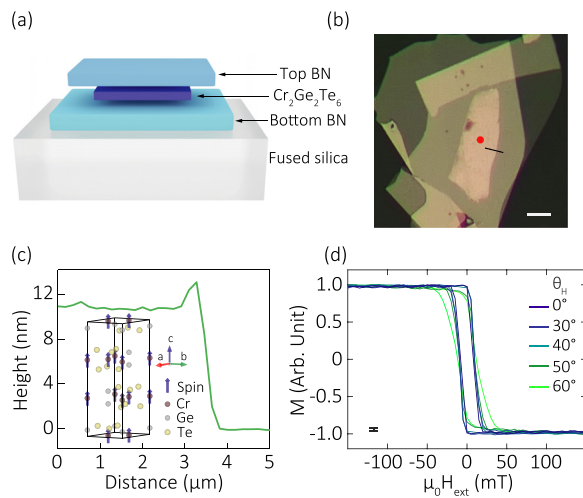
we record magnetization by means of Faraday rotation, which presents the magnetization component along the optical axis. The probe beam is focused on the sample in a cryostat by using an achromatic lens with a numerical aperture of 0.42, and the transmitted beam is re-collimated by another identical lens. The spatial resolution of this setup is estimated to be $d_0 = 2\,\mu m$ in Voigt geometry (i.e., $\theta_H = 90°$), and we expect that the beam focus is elliptically lengthened to be $d_0/\sin(\theta_H)$ along the tilted axis.

Figure 1(d) shows more magnetization hysteresis loops, which are obtained by changing θ_H to 30°, 40°, 50°, and 60°. The respective magnetic coercivity $H_c(\theta_H)$ is 9.5 ± 0.1 mT, 10.4 ± 0.1 mT, 12.4 ± 0.1 mT, and 16.0 ± 0.1 mT. Experimentally, the relation $H_c(0°) = H_c(\theta_H)\cos\theta_H$ is well followed, and this demonstrates that the field component in the out-of-plane direction dominates the magnetization reversal. These results are consistent with the previous findings that only the c axis is the easy axis in ferromagnetic $Cr_2Ge_2Te_6$ with perpendicular magnetic anisotropy.[22,23]

To study magnetization dynamics in the $Cr_2Ge_2Te_6$ ferromagnet, we have developed TRFR of a two-color pump–probe technique, which is schematically described in Fig. 2(a). The pump beam consists of a pulse train with a 78 MHz repetition rate generated by a
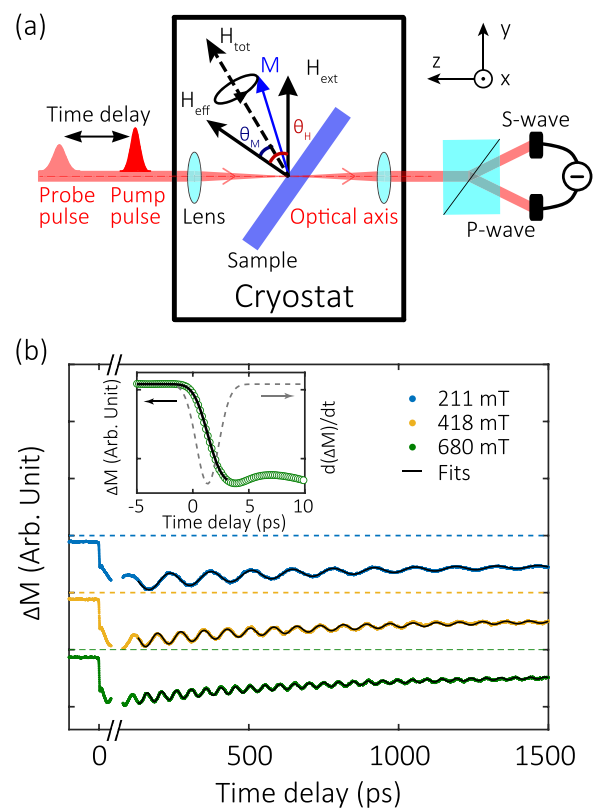
(a)

FIG. 1. (a) Schematic of a $Cr_2Ge_2Te_6$ flake encapsulated by two h-BN layers on a fused silica substrate and (b) optical micrograph of the $Cr_2Ge_2Te_6$ sample (scale bar: 15 μm). (c) Height profile measured by atomic force microscopy along the sample area. The inset is a schematic drawing of the unit cell for $Cr_2Ge_2Te_6$. (d) Magnetization hysteresis loops by varying θ_H at 10 K, where the scale bar on the lower left indicates the measurement error.

FIG. 2. (a) Schematic description of a two-color TRFR technique. (b) Normalized magnetization dynamics due to laser heating in $Cr_2Ge_2Te_6$ for different H_{ext} at $\theta_H = 50°$. Solid lines are fits and dashed lines are baselines in the absence of pumping. Inset: Magnetization dynamics (markers) and cumulative Gauss fit (line) in the first 10 ps (left axis). Dashed line (right axis) is the differential curve of the fit, which gives a time resolution of 1.2 ± 0.01 ps.

mode-locked Ti: sapphire laser, with a pulse width of 150 fs at a center wavelength of 770 nm. The probe beam with a sub-picosecond pulse width is produced by exciting a photonic crystal fiber by another sequence of synchronized ultrafast pulses to generate supercontinuum pulses[24] from which the probe beam is selected at 815 nm. Both the pump and probe beams are focused onto the sample surface by the same achromatic lens. The energy density of a single pump (probe) pulse is chosen to be constant at 123 μJ/cm^2 (2 μJ/cm^2). The time delay Δt between the pump and probe pulses is controlled by using a motorized translation stage to vary the optical path of the pump beam with respect to the probe beam. The intensities of the pump beam and the probe beam are modulated at 10 kHz and 83 Hz, respectively. The Faraday rotation of the probe beam is detected by a balanced bridge of photon receivers from which the signal is demodulated by applying a double-lock-in technique. The time resolution of the following pump–probe measurements is estimated to be 1.2 $\pm$ 0.01 ps [see the inset of Fig. 2(b)], and the spatial resolution is $d_0/\sin(\theta_H)$ as described above.

In an equilibrium state, as denoted in Fig. 2(a), the angle θ_M by which the magnetization deviates from the easy axis is determined by using $H_k\cos\theta_M\sin\theta_M = H_{ext}\sin(\theta_H - \theta_M)$,[25] where H_k is defined as $H_k = 2K_u/M_s - 4\pi M_s$, with K_u being defined as the uniaxial magnetic anisotropy energy along the c axis and M_s being the saturation magnetization. The out-of-plane effective field is $H_{eff} = H_k\cos\theta_M$, so the static magnetization remains along the total effective field $\mathbf{H}_{tot} = \mathbf{H}_{eff} + \mathbf{H}_{ext}$. Based on this relation, at a certain θ_H, θ_M asymptotically reaches θ_H by increasing H_{ext}, and in the case of a fixed H_{ext}, θ_M increases with θ_H.

An intensive optical pulse can remarkably perturb the magnetization of a ferromagnet.[26] Figure 2(b) plots the laser-induced magnetization dynamics up to 1500 ps for $\theta_H = 50°$ at three external fields: $H_{ext} = 211$, 418, and 680 mT. The inset presents the initial demagnetization dynamics in the first few picoseconds. This ultrafast process can be qualitatively understood by considering a drastic increase in the spin temperature leading to a reduction of both the magnetization $\mathbf{M}$ and the effective magnetic field $\mathbf{H}_{eff}$. As shown in Fig. 2(a), the total magnetic field $\mathbf{H}_{tot} = \mathbf{H}_{eff} + \mathbf{H}_{ext}$ is modified to tilt the magnetization $\mathbf{M}$ away from its equilibrium direction. After spin cooling of a few picoseconds,[27] $\mathbf{M}$ recovers its magnetization saturation value while the electron temperature cools through phonon emission. Meanwhile, $\mathbf{H}_{eff}$ recovers dynamically to the value at thermal equilibrium, so $\mathbf{M}$ recovers according to $\mathbf{H}_{tot} = \mathbf{H}_{eff} + \mathbf{H}_{ext}$ with spin precession.

The change $\Delta M(\Delta t)$ of magnetization dynamics probed by the Faraday rotation can be phenomenally described as $\Delta M(\Delta t) \sim \theta_F(\Delta t) = A_0 e^{-\Delta t/\tau_T}\cos(2\pi f\Delta t + \phi_0) + A_1 e^{-\Delta t/\tau_{P1}} + A_2 e^{-\Delta t/\tau_{p2}}$. The first term describes the spin-precession dynamics in which A_0, τ_T, f, and φ_0 denote the magnetization amplitude, the transverse spin relaxation time, the precession frequency, and the initial phase, respectively. The second and third terms describe the magnetization recovery process, where A_1 (A_2) and τ_{P1} (τ_{P2}) are, respectively, the demagnetization magnitude and the characteristic time constant of a short (long) process. By fitting the experimental data, we obtain the precession frequency as $f = 7.34 \pm 0.01$ GHz, 12.89 ± 0.01 GHz, and 20.32 ± 0.03 GHz, and $A_0 = 0.095 \pm 0.016$, 0.073 ± 0.087, and 0.055 ± 0.015 for $H_{ext} = 211$, 418, and 680 mT, respectively. The precession frequency clearly increases, while the oscillation magnitude decreases. Qualitatively, this coincides with the spin detection scenario described in Fig. 2(a), i.e., a large H_{ext} contributes to a larger H_{tot} giving rise to a larger precession frequency and simultaneously a larger θ_M, which in turn decreases the spin projection on the optical axis. In addition, we obtain the magnetization recovery-time constants $\tau_{p1} \approx 400 \pm 150$ ps and $\tau_{p2} \approx 8 \pm 2$ ns, which are similar for different H_{ext}. These two relaxation processes are quite likely related to energy relaxation by optical phonons and acoustic phonons in semiconductor structures at low temperatures.[28] For each curve, a cumulative heating effect is indicated at $\Delta t < 0$ by a clear offset from the dashed baseline.

To more systematically investigate the magnetization dynamics of this sample, TRFR measurements of H_{ext} dependence at various θ_H are performed and fitted by using the method described above. The frequency f and the transverse spin relaxation rate τ_T^{-1} as a function of the external magnetic field are shown in Figs. 3(a) and 3(b), respectively. To analyze the data more quantitatively, we use the expression $f = \gamma(H_1 H_2)^{1/2}/2\pi$ with a PMA based on the Kittel formula.[29] Here, $H_1 = H_{ext}\cos(\theta_M - \theta_H) + H_k\cos^2\theta_M$, $H_2 = H_{ext}\cos(\theta_M - \theta_H) + H_k\cos(2\theta_M)$, and $\gamma = g\mu_B/\hbar$, in which g, μ_B, and $\hbar$ are the spectroscopic splitting factor, the Bohr magneton, and the reduced Planck constant, respectively. In addition to using $H_k\cos\theta_M\sin\theta_M = H_{ext}\sin(\theta_H - \theta_M)$, we fit all curves of f vs H_{ext} by applying the same set of parameters H_k and g [see the solid lines in Fig. 3(a)]. We obtain $\mu_0 H_k = 125 \pm 8$ mT and a g factor of 2.04 ± 0.03. Based on the definition $H_k = 2K_u/M_s - 4\pi M_s$ and the previous measurement of $M_s = 192$ emu/cm^3,[21] we determine the magnetic anisotropy energy density $K_u = 3.4 \times 10^5$ erg/cm^3, which is similar to the value obtained by ferromagnetic resonance for bulk $Cr_2Ge_2Te_6$.[22,23] In addition, Fig. 3(c)
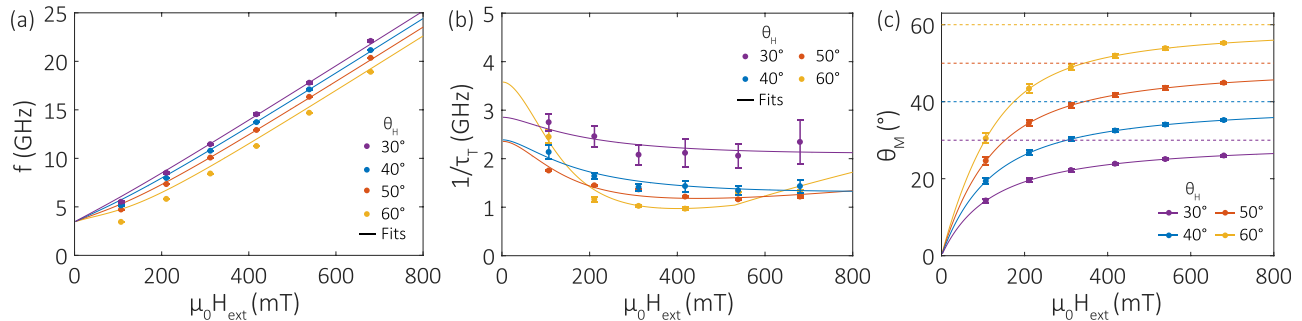

FIG. 3. Precession frequency f (a) and transverse spin relaxation rate τ_T^{-1} (b) vs H_{ext} at different θ_H. Markers denote experimental data and solid lines are fitted according to the Kittel formula. (c) Calculated equilibrium angle θ_M (markers and lines) vs H_{ext} at different θ_H (dashed lines).

plots the corresponding θ_M as a function of the external magnetic field, which is consistent with the scenario described in Fig. 2(a), i.e., θ_M increases to θ_H upon increasing H_{ext}.

As a key parameter in the Landau–Lifshitz–Gilbert equation, the damping coefficient is regarded to more conveniently describe the magnetization relaxation.[30] By combining the Landau–Lifshitz–Gilbert equation and the Kittel formula, the effective damping coefficient α_{eff} is given by the relation $\alpha_{eff} = 2/[\gamma\tau_T(H_1 + H_2)]$.[31] Figure 4 shows α_{eff} as a function of frequency f, which is obtained by using τ_T from Fig. 3(b) and θ_M from Fig. 3(c) to determine H_1 and H_2.

Despite the intrinsic damping coefficient α_0 being regarded independent of the external field, it clearly decreases with increasing precession frequency and approaches a constant value that is independent of H_{ext} and θ_H. For this point, we analytically decompose the effective damping coefficient into an intrinsic damping α_0 and an extrinsic damping α_{ext} (i.e., $\alpha_{eff} = \alpha_0 + \alpha_{ext}$), in which α_{ext} is due to inhomogeneous broadening and depends on f. Here, we propose the spatial fluctuations of the perpendicular magnetic anisotropy as the main extrinsic source, and we write $\alpha_{eff} = \alpha_0 + (2\ln2)^{1/2}[\gamma(H_1 + H_2)]^{-1}|d\omega/dH_k|\Delta H_k$ by using the expression derived in Ref. 32, where ΔH_k is the deviation of the PMA magnitude from H_k, and $|d\omega/dH_k|$ is numerically calculated by applying the Kittel formula. As shown by the solid lines in Fig. 4, α_{eff} is well fit with $\alpha_0 = 0.006 \pm 0.002$ and $\mu_0\Delta H_k = 8.0 \pm 2.0$ mT. The PMA deviation ΔH_k in this sample can be produced during crystal growth or in the preparation of the $Cr_2Ge_2Te_6$ flake, e.g., by introducing defects or forming terraces by exfoliation, and these local effects are present on a length scale of nanometers which is too far beyond the optical resolution to be distinguished. This inhomogeneous broadening is suppressed in the regime of a large H_{ext}, so α_{eff} approaches the intrinsic Gilbert damping coefficient for different θ_H.[33,34]

Note that the Gilbert damping constant $\alpha_0 = 0.006 \pm 0.002$ for this semi-insulating $Cr_2Ge_2Te_6$ is lower than that measured for many ferromagnetic materials with PMA.[32,33] This result may be qualitatively understood by considering two facts that are mostly absent in metallic ferromagnets. First, the deviation of the g factor of 2.04 ± 0.03
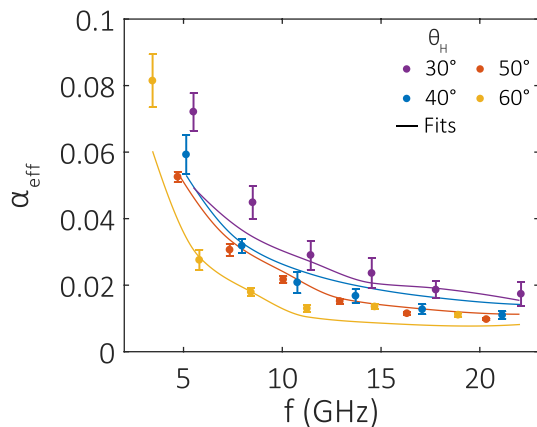
from the free-electron value $g = 2$ indicates a tiny orbital contribution to the magnetization. This points to a weak spin–orbit interaction, which induces spin–phonon scattering and thereby strongly suppresses the transverse magnetization relaxation.[35] In addition, since electrons are mostly localized in a semi-insulating system, spin relaxation due to electron–electron scatterings is highly suppressed in this layered $Cr_2Ge_2Te_6$.

In summary, we report herein the laser-induced magnetization dynamics of a 10.5 nm vdW ferromagnet. By using Kerr and Faraday rotations, we record the magnetization hysteresis loops at various θ_H and observe the PMA of the $Cr_2Ge_2Te_6$ nanoflake. The magnetization dynamics measured by the in-house-developed TRFR technique reveals an effective PMA field of $\mu_0H_k = 125 \pm 8$ mT and an intrinsic damping coefficient of $\alpha_0 = 0.006 \pm 0.002$. Experimentally, the effective damping coefficient is dominated by extrinsic inhomogeneous broadening in the regime of a small external magnetic field and it approaches an intrinsic damping coefficient at high external magnetic fields. We attribute the extrinsic damping to the inhomogeneous broadening of the PMA deviation, with $\mu_0\Delta H_k = 8.0 \pm 2.0$ mT. Both the low intrinsic damping coefficient and the PMA of the nanoflake make semi-insulating vdW ferromagnets candidates for low-dissipation magnetic devices, such as spin-transfer–torque magnetic random-access memory. Future studies of particular interest are to investigate the magnetization dynamics in a vdW magnet of a few atomic layers down to a monolayer.

DATA AVAILABILITY

The data that support the findings of this study are available from the corresponding author upon reasonable request.

FIG. 4. Effective damping α_{eff} calculated from τ_T, H_1, and H_2 vs precession frequency f at varied θ_H (markers). Solid lines are fits taking into account the deviation of PMA as described in the main text.

REFERENCES

[1]S. A. Wolf, D. D. Awschalom, A. Buhrman, J. M. Daughton, v Molnár, M. L. Roukes, A. Y. Chtchelkanova, and D. M. Treger, "Spintronics: A spin-based electronicsvision for the future," Science **294**, 1488 (2001).

[2]Y. K. Kato, R. C. Myers, A. C. Gossard, and D. D. Awschalom, "Observation of the spin Hall effect in semiconductors," Science **306**, 1910 (2004).

[3]J. Wunderlich, B. Kaestner, J. Sinova, and T. Jungwirth, "Experimental observation of the spin-Hall effect in a two-dimensional spin-orbit coupled semiconductor system," Phys. Rev. Lett. **94**, 047204 (2005).

[4]J. D. Koralek, C. P. Weber, J. Orenstein, B. A. Bernevig, S. C. Zhang, S. Mack, and D. D. Awschalom, "Emergence of the persistent spin helix in semiconductor quantum wells," Nature **458**, 610 (2009).

[5]M. P. Walser, C. Reichl, W. Wegscheider, and G. Salis, "Direct mapping of the formation of a persistent spin helix," Nat. Phys. **8**, 757 (2012).

[6]M. König, S. Wiedmann, C. Brüne, A. Roth, H. Buhmann, L. W. Molenkamp, X. L. Qi, and S. C. Zhang, "Quantum spin Hall insulator state in HgTe quantum wells," Science **318**, 766 (2007).

[7]C. Z. Chang, J. Zhang, X. Feng, J. Shen, Z. Zhang, M. Guo, K. Li, Y. Ou, P. Wei, L. L. Wang, Z. Q. Ji, Y. Feng, S. Ji, X. Chen, J. Jia, X. Dai, Z. Fang, S. C. Zhang, K. He, Y. Wang, L. Lu, X. C. Ma, and Q. K. Xue, "Experimental observation of the quantum anomalous Hall effect in a magnetic topological insulator," Science **340**, 167 (2013).

[8]V. Mourik, K. Zuo, S. M. Frolov, S. R. Plissard, E. P. A. M. Bakkers, and L. P. Kouwenhoven, "Signatures of Majorana fermions in hybrid superconductor-semiconductor nanowire devices," Science **336**, 1003 (2012).

[9] K. F. Mak, C. Lee, J. Hone, J. Shan, and T. F. Heinz, "Atomically thin MoS₂: A new direct-gap semiconductor," Phys. Rev. Lett. **105**, 136805 (2010).

[10] G.-B. Liu, D. Xiao, Y. Yao, X. Xu, and W. Yao, "Electronic structures and theoretical modelling of two-dimensional group-VIB transition metal dichalcogenides," Chem. Soc. Rev. **44**, 2643–2663 (2015).

[11] T. Song, X. Cai, M. W. Y. Tu, X. Zhang, B. Huang, N. P. Wilson, K. L. Seyler, L. Zhu, T. Taniguchi, K. Watanabe, M. A. McGuire, D. H. Cobden, D. Xiao, W. Yao, and X. Xu, "Giant tunneling magnetoresistance in spin-filter van der Waals heterostructures," Science **360**, 1214 (2018).

[12] K. F. Mak, K. L. McGill, J. Park, and P. L. McEuen, "The valley Hall effect in MoS₂ transistors," Science **344**, 1489 (2014).

[13] E. Barré, J. A. C. Incorvia, S. H. Kim, C. J. McClellan, E. Pop, H. S. P. Wong, and T. F. Heinz, "Spatial separation of carrier spin by the valley Hall effect in monolayer WSe₂ transistors," Nano Lett. **19**, 770 (2019).

[14] Q. Shao, G. Yu, Y. W. Lan, Y. Shi, M. Y. Li, C. Zheng, X. Zhu, L. J. Li, P. Khalili Amiri, and K. L. Wang, "Strong Rashba-Edelstein effect-induced spin−orbit torques in monolayer transition metal dichalcogenide/ferromagnet bilayers," Nano Lett. **16**, 7514 (2016).

[15] X. Wang, J. Tang, X. Xia, C. He, J. Zhang, Y. Liu, C. Wan, C. Fang, C. Guo, W. Yang, Y. Guang, X. Zhang, H. Xu, J. Wei, M. Liao, X. Lu, J. Feng, X. Li, Y. Peng, H. Wei, R. Yang, D. Shi, X. Zhang, Z. Han, Z. Zhang, G. Zhang, G. Yu, and X. Han, "Current-driven magnetization switching in a van der Waals, ferromagnet Fe₃GeTe₂," Sci. Adv. **5**, eaaw8904 (2019).

[16] C. Gong, L. Li, Z. Li, H. Ji, A. Stern, Y. Xia, T. Cao, W. Bao, C. Wang, Y. Wang, Z. Q. Qiu, R. J. Cava, S. G. Louie, J. Xia, and X. Zhang, "Discovery of Intrinsic ferromagnetism in two-dimensional van der Waals crystals," Nature **546**, 265 (2017).

[17] B. Huang, G. Clark, E. Navarro-Moratalla, D. R. Klein, R. Cheng, K. L. Seyler, D. Zhong, E. Schmidgall, M. A. McGuire, D. H. Cobden, W. Yao, D. Xiao, P. Jarillo-Herrero, and X. Xu, "Layer-dependent ferromagnetism in a van der Waals crystal down to the monolayer limit," Nature **546**, 270 (2017).

[18] Y. Deng, Y. Yu, Y. Song, J. Zhang, N. Z. Wang, Z. Sun, Y. Yi, Y. Z. Wu, S. Wu, J. Zhu, J. Wang, X. H. Chen, and Y. Zhang, "Gate-tunable room-temperature ferromagnetism in two-dimensional Fe₃GeTe₂," Nature **563**, 94 (2018).

[19] B. Huang, G. Clark, D. R. Klein, D. MacNeill, E. Navarro-Moratalla, K. L. Seyler, N. Wilson, M. A. McGuire, D. H. Cobden, D. Xiao, W. Yao, P. Jarillo-Herrero, and X. Xu, "Electrical control of 2D magnetism in bilayer CrI₃," Nat. Nanotechnol. **13**, 544 (2018).

[20] S. Jiang, L. Li, Z. Wang, K. F. Mak, and J. Shan, "Controlling magnetism in 2D CrI₃ by electrostatic doping," Nat. Nanotechnol. **13**, 549 (2018).

[21] Z. Wang, T. Zhang, M. Ding, B. Dong, Y. Li, M. Chen, X. Li, J. Huang, H. Wang, X. Zhao, Y. Li, D. Li, C. Jia, L. Sun, H. Guo, Y. Ye, D. Sun, Y. Chen, T.

Yang, J. Zhang, S. Ono, Z. Han, and Z. Zhang, "Electric-field control of magnetism in a few-layered van der Waals ferromagnetic semiconductor," Nat. Nanotechnol. **13**, 554 (2018).

[22] X. Zhang, Y. Zhao, Q. Song, S. Jia, J. Shi, and W. Han, "Magnetic anisotropy of the single-crystalline ferromagnetic insulator Cr₂Ge₂Te₆," Jpn. J. Appl. Phys., Part 1 **55**, 033001 (2016).

[23] J. Zeisner, A. Alfonsov, S. Selter, S. Aswartham, M. P. Ghimire, M. Richter, J. van den Brink, B. Büchner, and V. Kataev, "Magnetic anisotropy and spin-polarized two-dimensional electron gas in the van der Waals ferromagnet Cr₂Ge₂Te₆," Phys. Rev. B **99**, 165109 (2019).

[24] See https://www.newport.com.cn/medias/sys_master/images/images/ha8/ha9/8797285449758/Supercontinuum-Generation-in-SCG-800-App-Note-28.pdf for "generating supercontinuum light."

[25] W. He, H. Liu, H. Wu, J. Cai, and Z. Cheng, Appl. Phys. Lett. **106**, 042401 (2015).

[26] E. Beaurepaire, J. C. Merle, A. Daunois, and J.-Y. Bigot, Phys. Rev. Lett. **76**, 4250 (1996).

[27] M. van Kampen, C. Jozsa, J. T. Kohlhepp, P. LeClair, L. Lagae, W. J. M. de Jonge, and B. Koopmans, "All-optical probe of coherent spin waves," Phys. Rev. Lett. **88**, 227201 (2002).

[28] J. Shah, *Ultrafast Spectroscopy of Semiconductors and Semiconductor Nanostructures*, 2nd ed. (Springer-Verlag, Berlin Heidelberg, 1999), pp. 9–11.

[29] S. Mizukami, E. P. Sajitha, D. Watanabe, F. Wu, T. Miyazaki, H. Naganuma, M. Oogane, and Y. Ando, "Gilbert damping in perpendicularly magnetized Pt/Co/Pt films investigated by all-optical pump-probe technique," Appl. Phys. Lett. **96**, 152502 (2010).

[30] A. Sakuma, "Microscopic description of Landau-Lifshitz-Gilbert type equation based on the s-d model," arXiv:cond-mat/0602075 (2006).

[31] C. E. Patton, "Linewidth and relaxation processes for the main resonance in the spin-wave spectra of Ni-Fe alloy films," J. Appl. Phys. **39**, 3060 (1968).

[32] S. Iihama, S. Mizukami, H. Naganuma, M. Oogane, Y. Ando, and T. Miyazaki, "Gilbert damping constants of Ta/CoFeB/MgO(Ta) thin films measured by optical detection of precessional magnetization dynamics," Phys. Rev. B **89**, 174416 (2014).

[33] D. M. Lattery, D. Zhang, J. Zhu, X. Hang, J. P. Wang, and X. Wang, "Low gilbert damping constant in perpendicularly magnetized W/CoFeB/MgO films with high thermal stability," Sci. Rep. **8**, 13395 (2018).

[34] R. Arias and D. L. Mills, "Extrinsic contributions to the ferromagnetic resonance response of ultrathin films," Phys. Rev. B **60**, 7395 (1999).

[35] J. Pelzl, R. Meckenstock, D. Spoddig, F. Schreiber, J. Pflaum, and Z. Frait, "Spin−orbit-coupling effects on g-value and damping factor of the ferromagnetic resonance in Co and Fe films," J. Phys.: Condens. Matter **15**, S451 (2003).